Received May 28, 2021, accepted May 31, 2021, date of publication June 4, 2021, date of current version June 14, 2021.

Digital Object Identifier 10.1109/ACCESS.2021.3086217

Optical Design and Investigation of a Dual-Interference Channels and Bispectrum Static Fourier-Transform Imaging Spectrometer Based on Stepped Micro-Mirror

JUN REN[1,2], JINGUANG LÜ[1], BAIXUAN ZHAO[1,2], QIANG WANG[1], YUXIN QIN[1,2], JIN TAO[1], JINGQIU LIANG[1], AND WEIBIAO WANG[1]

[1]State Key Laboratory of Applied Optics, Changchun Institute of Optics, Fine Mechanics and Physics, Chinese Academy of Sciences, Changchun 130033, China
[2]College of Materials Science and Opto-Electronic Technology, University of Chinese Academy of Science, Beijing 100049, China

Corresponding authors: Jingqiu Liang (liangjq@ciomp.ac.cn) and Jinguang Lü (jinguanglv@163.com)

This work was supported in part by the National Natural Science Foundation of China under Grant 61627819, Grant 61805239, Grant 61727818, and Grant 62005267; in part by the Jilin Scientific and Technological Development Program under Grant 20190303063SF, Grant 20150520101JH, and Grant 20180201024GX; in part by the Youth Innovation Promotion Association of the Chinese Academy of Sciences under Grant 2018254; and in part by the National Key Research and Development Program of China under Grant 2019YFB2006000.

ABSTRACT We demonstrate a novel tempo-spatial mixed-modulation Fourier-transform infrared imaging spectrometer. The static interference channel based on a stepped micro-mirror contributes a compact system with high stability. The instrument functions in two spectral bands ranging between 3.7–4.8 μm and 7.7–9.3 μm, and the spectral resolution of the dual-interference channels achieves 51.5 and 4.1 cm^{-1}, respectively. The instantaneous field of view is 0.15 mrad, and the working F/1.93 enables high optical throughput. The optical design and tolerance are presented with experimental investigation results, showing attractive potential in remote sensing application.

INDEX TERMS Infrared imaging spectrometer, fourier-transform, tempo-spatial mixed-modulation, stepped micro-mirror, optical design.

I. INTRODUCTION

Capable of simultaneously obtaining images and spectral information [1], [2], imaging spectrometry is widely used as a non-contact detection instrument in environmental pollution monitoring, hazardous gas detection, and aerospace remote sensing [3]–[6]. Many harmful gases have strong absorption peaks in the infrared region, e.g, CO_2 has a strong absorption peak at 4.3 μm, SO_2 at 7.4 μm, and NH_3 at 8.3 μm, which means that the infrared is an important and effective region for pollutants monitoring. Fourier-transform imaging spectrometers (IFTS) are based on the principle of the Michelson interferometer [7]–[9]. The different modulation methods can be divided into temporal modulation, spatial modulation, and tempo-spatially mixed modulation (TSMIFTS) [10], [11]. TSMIFTS does not require a precision moving mirror system or a slit that restricts the luminous flux. Conversely, it has advantages of high throughput, resolution, stability and a fast response, which lead to increasing research attention.

In 2011, Matallah *et al.* designed a Fourier-transform imaging spectrometer [12]; the mirror of the Michelson interferometer was replaced by a corner mirror to realize a compact structure, and a spectral resolution of 25 cm^{-1} was obtained in 3–5 μm. In 2018, Yan *et al.* proposed a high-resolution channel imaging spectral polarimeter using a liquid crystal variable retarder (LCVR) [13], [14], the simulation experiment results showed that in the working range of 0.48–0.96 μm, the theoretical resolution of the spectrum could reach 40 cm^{-1}. In 2019, Michael *et al.* proposed a mid-wave infrared hyperspectral imager based on a single-mirror interferometer structure [15]–[18], the hyperspectral data cube was obtained by the windowing method, and a spectral resolution of 12 cm^{-1} was achieved in 3.8–13 μm.

The above studies show that a wide-band, high-spectral resolution infrared imaging spectrometer is of significant

The associate editor coordinating the review of this manuscript and approving it for publication was Norbert Herencsar.

interest. At present, most reported TSMIFTS function in the visible/near-infrared band, and their spectral resolution needs to be improved. This work proposes a dual-interference channel and bispectrum static TSMIFTS. The instrument has the following characteristics: (1) a stepped micro-mirror is used to replace the moving mirror system, which provides the advantages of a compact structure and high stability; (2) the bispectrum design satisfies the requirements for infrared fingerprint identification of most pollutants, and the design of dual-interference channels enables rapid qualitative and quantitative analysis of substances; and (3) the athermalized design of the opto-mechanical structure allows the instrument to realize higher environmental adaptability. This paper provides the basic working principle of the instrument and reports the optical design, laboratory calibration, and experimental test results.

II. SPECIFICATIONS AND OPTICAL DESIGN

A. BASIC WORKING PRINCIPLE

Figure 1 depicts the basic structure of the TSMIFTS, consisting of a front common-aperture telescope, dual-interference modules, a medium-wave infrared (MWIR) and long-wave infrared (LWIR) rear imaging system, and a folding mirror to realize a compact structure. Here, the dual-interference module integrates a high-resolution interference channel and a broad-band interference channel. Two stepped micro-mirrors with different step heights are used in the two interference channels to generate optical path differences (OPD). The selection of the interference channel is realized by controlling the switch mirror pair. The working principle is as follows: the light emitted by the target enters the front common-aperture telescope at different angles of view; it is then split by the beam splitting system and imaged on the plane mirror and the stepped micro mirror. The step height difference leads to the conjugate image points on the plane mirror and the stepped micro-mirror at the same step sequence to have a fixed phase difference. Then, these two coherent image points are used as the object points of the rear imaging system and are again imaged on the focus plane array (FPA), and the corresponding interferogram is generated at the same time. A dichroic mirror is used to separate the MWIR and LWIR for detection, and medium wavelength is reflected while the long wavelength is transmitted. The filter is placed in front of the detector window. By using circumferential scanning, the target enters the system with different field angles and is imaged on the adjacent sub-step reflective surface. This scanning angle interval needs to be accurately calculated; during scanning, it needs to be ensured that the scanning direction is consistent with the direction of the step height difference, and the complete interference sequence of the target can be obtained after the entire scanning period is completed. A discrete Fourier transform is performed on this interference sequence to obtain the spectral information of the object point. By cutting and stitching a series of scanned images with interference fringes, a panoramic two-dimensional image of the target can be thus obtained.

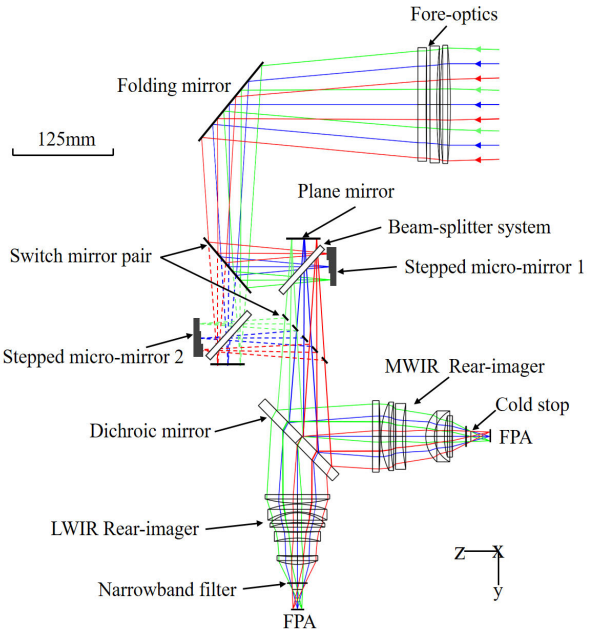

FIGURE 1. Schematic diagram of the dual-interference channels and bispectrum static TSMIFTS.

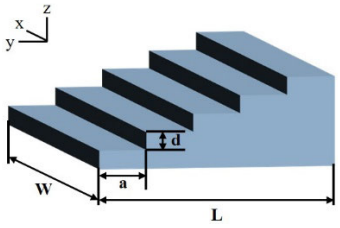

FIGURE 2. Schematic diagram of the stepped micro-mirror.

The stepped micro-mirror is used to generate the OPD. Figure 2 shows a schematic diagram of the stepped micro-mirror. The length of the stepped micro-mirror is L, the width is W, the width of the sub-step reflection surface is a, and the step height is d. Therefore, the OPD is determined by the height d and the number of steps n:

$$\delta(n) = 2nd \tag{1}$$

The OPD of the interference system is equal to 2 times the total height of the steps. For the TSMIFTS proposed in this paper, the interference light field is cut into N units along the y direction of the stepped micro-mirror. Every unit of the same step sequence has the same optical path. The detector obtains interference fringes in the y direction. The relationship between the interference intensity and the interference order is given by the following equation:

$$I[x, y, \delta(n)] = \int B(x, y, v) \exp[j2\pi v\delta(n)]dv \tag{2}$$

where $v = 1/\lambda$ is the wave number, and the spectral information of the target point can be obtained by performing a discrete Fourier transform on the interference sequence $\delta(n)$

corresponding to the target point (x, y):

$$B(x, y, v) = 2d \sum_{n=0}^{N-1} I(x, y, n) \exp(-j2\pi v2nd) \tag{3}$$

B. PERFORMANCE AND DESIGN SPECIFICATIONS

The performance and design parameters of TSMIFTS are summarized in Table 1. The working spectral regions of the system are between 3.7–4.8 μm and 7.7–9.3 μm. To realize qualitative analysis of the target, the spectral resolution of the broad-band channel was set to 50 cm^{-1}; for quantitative analysis of the target concentration, the spectral resolution of the high-resolution channel was set to 3.2 cm^{-1}. The detection distance was 200−2000 m, and the spatial pixel resolution at 2000 m was 0.3 m. The system field of view (FOV) was 2.75 × 2.2°, and the instantaneous field of view (IFOV) in the scanning direction was 0.15 mrad. Two cooled HgCdTe infrared detectors with 320 × 256 pixel array was used in the medium and long wave imaging channels, respectively. The pixel size was 30 μm × 30 μm and the working temperature of the detector was 77 k. The working F−number was 1.93 to ensure high throughput of the system.

TABLE 1. Specifications of FTIS.

Parameters	Value
Spectral range	3.7–4.8 μm, 7.7–9.3 μm
Spectral resolution	50 cm^{-1}, 3.2 cm^{-1}
Focusing rang	200–2000 m
Spatial resolution	0.3 m
FOV	2.75×2.2°
IFOV	0.15 mrad
Detector array size	320× 256
Pixel size	30×30 μm
Detector temperature	77 K
Working F-number	1.93

C. INTERFERENCE CHANNEL DESIGN

In the broad-band interference channel, based on the classical Nyquist-Shannon sampling theorem [19], [20], the sampling frequency of the interference system should be greater than 2 times the highest input frequency:

$$F_s \geq 2f_H \tag{4}$$

where F_s is the system sampling frequency, and its value is equal to $1/2d_1$; $f_H = 1/\lambda_{min}$. The minimum working wavelength of the instrument is $\lambda_{min} = 3.7$ μm, so the sampling interval, i.e. the step height, must satisfy $d_1 \leq \lambda_{min}/4 = 0.925$ μm, the lowest sampling frequency $F_s \geq 2/\lambda_{min} = 5405$ cm^{-1}. To ensure a certain margin, a step height of $d_1 = 0.625$ μm and sampling frequency of $F_s = 1/2d_1 = 8000$ cm^{-1} are determined. The relationship between spectral resolution and OPD is given by:

$$\Delta v = \frac{1}{\delta_{\max}} \tag{5}$$

Based on Eq. (1) and Eq. (5), to achieve a spectral resolution of 50 cm^{-1}, the number of steps is $N = 1/2d_1\Delta v = 160$.

For high-resolution interference channels, a large-step structure was used to increase the OPD. When the number of steps is $N = 160$ and the height of the steps is $d_2 = 10$ μm, the spectral resolution $\Delta v = 1/2nd_2 = 3.125$ cm^{-1}. At this time, the sampling frequency of the system is $F_s = 1/2d_2 = 500$ $cm^{-1} \ll 5405$ cm^{-1}, and the classical sampling criteria are no longer applicable. To avoid aliasing of the reconstructed spectrum, a narrow-band filter was placed before the detector to filter the input signal into a bandpass signal. The sampling frequency F_s of the bandpass signal is given by the following equation:

$$\frac{2f_H}{K} \leq F_s \leq \frac{2f_L}{K-1}, \quad K \leq \frac{f_H}{BW} \tag{6}$$

where BW is the input signal bandwidth, f_L represents the lowest input frequency, and K is any integer less than or equal to f_H/BW. Based on the sampling theorem of bandpass signals, the sampling frequency F_s depends on the signal bandwidth BW and the center wavelength (CWL). Choose filters with a suitable BW and center frequency to make the sampling frequency F_s meet the above formula enable sampling below the Nyquist frequency. The filter parameters for recognition of common polluting gases are shown in Table 2.

TABLE 2. Narrow-band filter specifications.

CWL/nm	Value	Material	Thickness/mm
4120	80	Sapphire	1
4275	50	Sapphire	1
4515	90	Sapphire	1
4685	95	Sapphire	1
8242	150	Ge	1
8688	180	Ge	1
8834	210	Ge	1
8940	265	Ge	1

The specific parameters of the small-step micro-mirror and the large-step micro-mirror used in this work are shown in Table 3. Because the two step mirrors share the same imaging system, the other parameters are the same except the step height d that determines the OPD is different. The size of the stepped micro-mirror is 32 mm × 25.6 mm, the number of steps is $N = 160$, the step height $d_1 = 0.625$ μm, $d_2 = 10$ μm, the length of the sub-step surface $L = 25.6$ mm, and the width is $a = 0.2$ mm. To ensure complete acquisition of interference information, we set the number of pixels corresponding with the width of the sub-step surface to 2, and the pixel size of the detector was $p = 30$ μm, hence,

TABLE 3. Stepped micro-mirror specifications.

Parameters	Small-step micro-mirror	Small-step micro-mirror
Stepped micro-mirror size	32 mm×25.6 mm	32 mm×25.6 mm
Step numbers	160	160
Step height	0.625 μm	10 μm
Sub-Step width	0.2 mm	0.2 mm
Sub-Step length	25.6 mm	25.6 mm

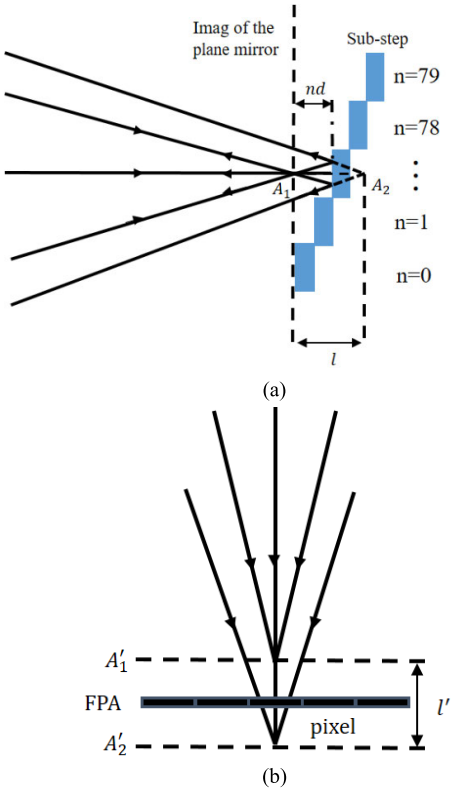

FIGURE 3. The imaging process on stepped surface and plane mirror (a) defocus caused by stepped structure and (b) interference and imaging process on FPA.

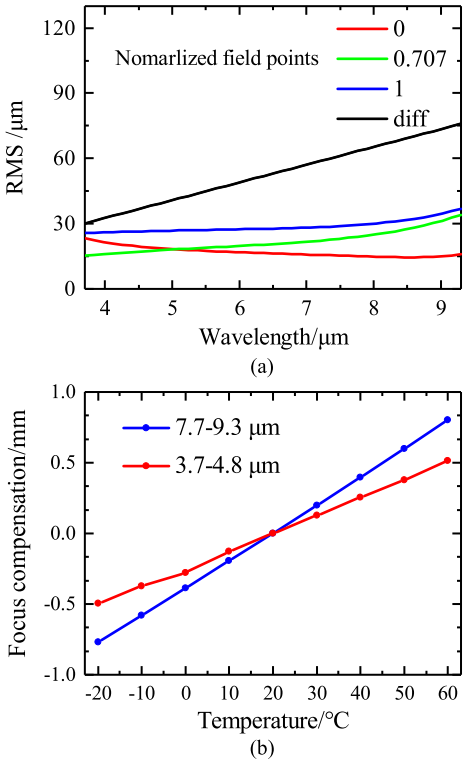

FIGURE 4. Design results of the fore-optics (a) spot diagram in the 3.7–9.3 μm spectral range and (b) the temperature focusing compensation in the MWIR and LWIR.

the vertical magnification of the rear imaging system can be obtained as $\beta_{rear} = 2 \times p/a = 2 \times 30\ \mu\text{m}/0.2\ \text{mm} = 0.3$.

D. IMAGING ANALYSIS

The stepped structure would cause corresponding defocusing of the image points on different steps, resulting in a decrease in the quality of the final image. Figure 3(a) shows the imaging process of the front imaging system on the plane mirror and the corresponding Nth sub-step. A_1 is the real image point, which is imaged on the step mirror. A_2 is the virtual image point, which is imaged at the mirror position of the plane mirror relative to the sub-step. The defocus generated by the sub-step is $\delta_{defocus} = nd$, and the distance is $l = 2nd$, where $n \in (-N/2, N/2-1)$. The middle sub-step is generally set at the 0-level, and the image of the plane mirror and the position of the sub-step surface coincide at this point. Based on the wave aberration theory and the Rayleigh criterion, when the maximum defocus of the optical system is less than the focal depth of the optical system $\sigma = 2\lambda F\#^2$, the image can be regarded as clear, where $F\#$ is the working F number of the imaging system. The working F number of the rear imaging system is $F^{\#}_{rear} = 1.93$; then, the working F number of the front imaging system $F^{\#}_{front} = F^{\#}_{rear}/\beta = 1.93/0.3 = 6.43$. The calculated minimum focal depths of the front imaging system for the MWIR and LWIR are 0.306 and 0.637 mm, respectively. There is a maximum defocus between the edge sub-step and the plane mirror, which is 0.05 and 0.8 mm for the MWIR and LWIR bands, respectively.

A_1 and A_2 are the coherent object points of the rear imaging system, and the secondary imaging process is shown in Figure 3(b). The position of the Gaussian image plane corresponding to A_1 is A_1', and the position of the Gaussian image plane corresponding to A_2 is A_2'. To balance the speckle size of the image points on the two Gaussian image planes in the same pixel, the FPA needs to be placed at the midpoint of the two Gaussian image planes. Based on the relationship between the axial magnification and the vertical magnification of the rear imaging system $\alpha = \beta^2$, there is a distance $l' = \alpha \cdot l = 2\beta^2 nd$. From the calculations, the minimum focal depths of the rear imaging system for the MWIR and LWIR are 0.027 and 0.057 mm,

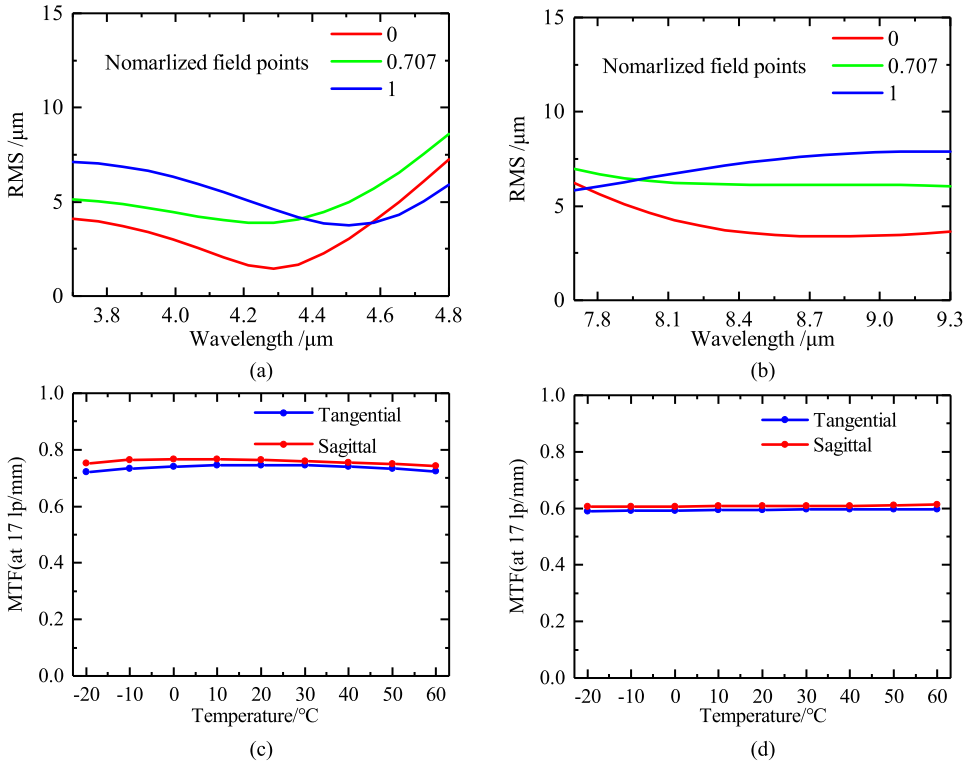

FIGURE 5. Results for the integrated optical system (a) spot diagram of the MWIR, (b) spot diagram of the LWIR, (c) MTF drift in the MWIR, and (d) MTF drift in LWIR.

respectively, and the maximum defocus corresponding to the small-step micro-mirror and the large-step micro-mirror are 0.0045 and 0.072 mm, respectively. The above results show that the defocus of the small-step micro-mirror is within the focal depth of the imaging system, while the defocus of the large-step micro-mirror is greater than the focal depth of the front imaging system, and the image quality on the edge sub-step mirror is reduced. To obtain high-quality stitched images, we selected the images on the 0-level sub-step for stitching.

E. OPTICAL DESIGN

For the TSMIFTS proposed in this paper, the optical system consists of a common-aperture telescope and rear imaging system. We designed the two parts separately, and then integrated and optimized them. The beam splitting system is equivalent to two parallel plates placed in the optical path with an angle of 45°, which would cause large astigmatism, hence, a cylinder is used in each sub-system to balance the aberration. Because the dichroic mirror reflects MWIR and transmits LWIR, the dichroic mirror should also be considered when designing the LWIR rear imaging system. A ZnSe beam splitter and a ZnSe dichroic mirror are used for high transmittance in both bands. The optical components and mechanical structure are affected by the ambient temperature. The front imaging system adopts an active focusing method to compensate for defocusing, and the MWIR and LWIR rear imaging systems adopt a passive a thermal design.

The spot diagram of the common-aperture telescope is shown in Figure 4(a). In the 3.7–9.3 μm spectral range, the RMS radii of the image points in the normalized field of view of 0, 0.7, and 1 are all smaller than the diffraction limit. The compact three-piece structure is achromatic in a broadband range. The relationship between the focus compensation of the common-aperture telescope and temperature is shown in Figure 4(b). The MWIR temperature focus compensation is $\pm$0.5 mm and it is $\pm$0.8 mm for the LWIR.

To improve the accuracy of ray tracing, we set the detector cold diaphragm as the aperture diaphragm of the integrated optical system to ensure 100% cold diaphragm matching. The design results of the integrated optical system are shown in Figure 5. The maximum RMS radius of the normalized field of view for the two wavebands is 9.8 μm, which is $<$15 μm (the half-size of a single pixel). At a temperature of 20 °C, the system modulation transfer function (MTF) value exceeds 0.71 and 0.59 for the MWIR and LWIR bands, respectively, and the MTF drift of the system is $<$0.025 within the temperature range of $-$20 to 60 °C, which shows that the optical system is temperature insensitive. The surfaces of all the lenses of the optical system are coated with a broadband anti-reflection coating. The average transmittance of the three lenses of the common-aperture telescope is $>$97.5% in the spectral range of 3.7$-$4.8 μm and 7.7$-$9.3 μm. The average transmittance of the lenses of the MWIR and LWIR rear imaging systems in the working spectrum is $>$98.2% and $>$98%, respectively, enabling the high luminous flux of the system.

III. TOLERANCE

A. TOLERANCES OF THE IMAGING SYSTEM

The back working distance of the common-aperture telescope and the rear imaging system was used to compensate for deviation of the optical system during processing and assembly, and the diffraction MTF was used as the standard for evaluation of the imaging system tolerance. After switching the ray aiming on, the tolerance sensitivities were obtained by running Monte Carlo analysis, the tightest offenders was the first len of the common-aperture telescope. The surface tilt is about 20″ and the element tilt is about 40″. In general, the tolerance of the imaging system is feasible. The MTF values for the MWIR and LWIR channels at the characteristic frequency of 17mm/lp have a 90% probability of being greater than 0.55 and 0.48, respectively.

B. TOLERANCES OF INTERFERENCE SYSTEMS

The core components of the interference system are plane mirrors and stepped micro-mirrors. The static interference structure avoids random and dynamic tilt errors generated by the moving mirror system during motion [21]. However, because of accuracy limitations during assembly, the plane mirrors and stepped micro-mirrors always have tilt error angles. Since the error caused by the tilt of the plane mirror and the stepped micro-mirror are equivalent, figure 6(a) shows the situation when the interference system has a tilt error, and the dotted line represents a tilted plane mirror. The tilt direction of the plane mirror is along the direction of the step height difference, the beam diameter is equal to the length L of the stepped micro-mirror, the angle between the ideal plane and the inclined plane is θ, and the intersection of the optical axis and the plane mirror is O, then, the OPD offset Δ is given by:

$$\Delta = \tan\theta \cdot x \tag{7}$$

where x is the distance from the optical axis and the value range is $x \in (-L/2, L/2)$. Substituting Eq. (7) into Eq. (1), the OPD becomes:

$$\delta'(n) = 2nd + 2\tan\theta \cdot x \tag{8}$$

It can be seen from Eq. (8) that under the influence of tilt error, the OPD at different positions x on the same step level is no longer a fixed value. On substituting Eq. (8) into Eq. (2), for monochromatic light with a wavelength of λ, an interference sequence with a tilt error is obtained:

$$\begin{aligned} I'\left(x, y, \delta'(n)\right) &= \frac{1}{a}\int_{na}^{(n+1)a} B(v)\exp\left\{j2\pi v\cdot\left[2nd + 2tan\theta\cdot x\right]\right\}dx \\ &= \sin c\left(2\pi va\tan\theta\right)\cdot B(v) \\ &\quad\times \exp\left\{j2\pi v\cdot\left[2n(d + a\cdot tan\,\theta) + \tan\theta\cdot a\right]\right\} \end{aligned} \tag{9}$$

Interferogram modulation depth M:

$$M = \sin c(2\pi va\tan\theta) \tag{10}$$

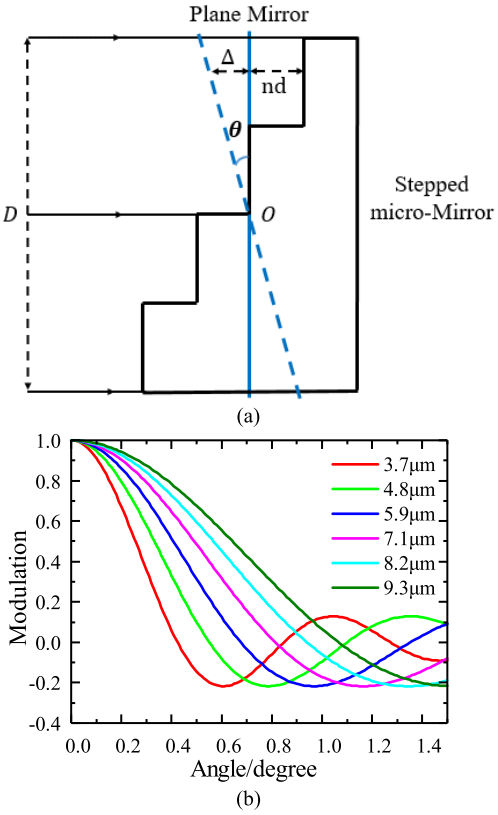

FIGURE 6. (a) Schematic diagram of interference system with tilt error and (b) relation curve of the inclination angle θ to the modulation depth over the working range 3.7–9.3 μm.

Initial phase of the interferogram φ_0:

$$\varphi_0 = 2\pi va\tan\theta \tag{11}$$

where $a = 0.2$mm is the width of the sub-step. Equation (10) shows that when there is a tilt error in the interferometric system, the cosine component of the interferogram received by the detector is modulated by $sinc(2\pi vatan\theta)$, resulting in a decrease in the modulation of the interferogram. Equation (11) shows that there is an initial phase error term $\varphi_0 = 2\pi vatan\theta$ in the cosine component, which leads to a decrease in the signal-to-noise ratio (SNR) of the interferogram. The modulation error and phase error in the interferogram are not related to the step height d and only related to the incident wavelength λ and the sub-step width a. Therefore, the calculated tilt angle tolerance is applicable to two interference channels. Figure 6(b) shows the relationship between the tilt angle and the degree of modulation at different wavelengths, taking the interferogram modulation degree reduced by up to 90% of the ideal state as a reference: $M \geq 0.9$. The maximum tilt angle allowed by the interference system is obtained at the wavelength $\lambda_{min} = 3.7$ μm, the tilt angle $\theta_{max} = 0.133°$.

The initial phase would cause the period of the interferogram to change and cause a reduction in the SNR. The period change of the interferogram caused by the initial phase should

be less than λ/SNR:

$$\frac{\varphi_0}{2\pi v} \leq \frac{\lambda}{SNR} \tag{12}$$

To ensure the accuracy of spectrum restoration, the SNR threshold was set to 100, and the maximum tilt angle was obtained at a wavelength of $\lambda_{min} = 3.7\ \mu$m, the tilt angle $\theta_{max} = 0.01^\circ = 36''$. Compared with decreased modulation, the phase error was more sensitive to the tilt angle, but it was still acceptable for assembly.

IV. EXPERIMENT AND RESULT ANALYSIS

A. SYSTEM PROCESSING AND TESTING OF THE STEPPED MICRO-MIRROR

Here, 3D laser confocal scanning microscopy (LSCM) VK-X1000 was used to measure the step height and surface topography of the small-step and large-step micro-mirrors. The total length of the scan was 32 mm and the scan range covered all the steps. The partial scan results of the stepped micro-mirror are shown in Figure 7. The measurement parameters are summarized in Table 4.

TABLE 4. Measured parameters of the stepped micro-mirror.

Measured Parameters	Small-step micro-mirror	Larger-step micro-mirror
Average sub-step height/μm	0.6187	9.982
Standard deviation/μm	0.0307	0.0413
Surface roughness/μm	0.0255	0.0336

B. MECHANICAL DESIGN AND ASSEMBLY

The imaging spectrometer was composed of a front common-aperture telescope, a dual-interference module, and a rear imaging system. These three independent systems were assembled on the main frame. The pitch axis of the U-shaped support arm coincides with the center of gravity of the instrument. The electric turntable allows the instrument to be adjusted and enables surrounding vision, as shown in Figure 8.

The main principles of the assembly and alignment of the system are as follows. First, the mechanical brackets and optical elements are fabricated and tested to ensure that they meet the designed tolerances. Then, the three systems are assembled and aligned, and interferometry is used to calibrate the angle deviation of the three cylindrical lenses and test the parallelism of the flat plates and the mirrors in the dual-interference module. These three systems are then integrated into the main frame and aligned with the compensator for a good performance.

C. SPECTRAL CALIBRATION

Eight narrow-band filters with known wavenumber positions in Table 2 were used to calibrate the high-resolution interference channel and the broad-band interference channel.

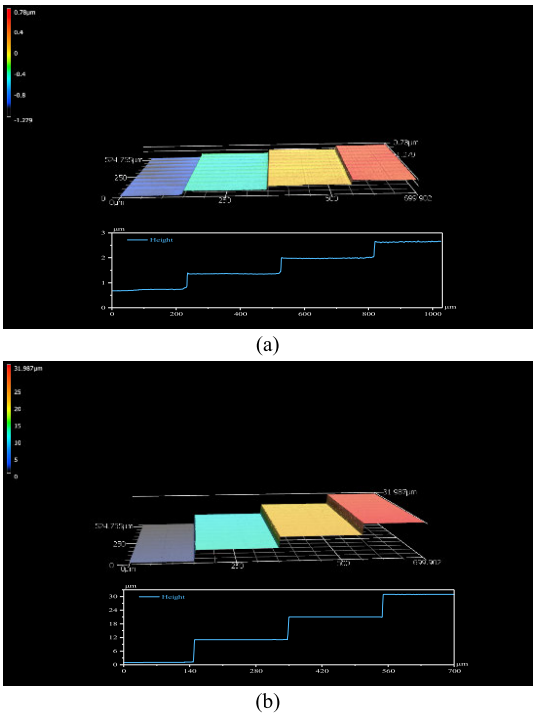

(a) (b)

FIGURE 7. LSCM local scanning results of (a) small-step micro-mirror and (b) large-step micro-mirror.

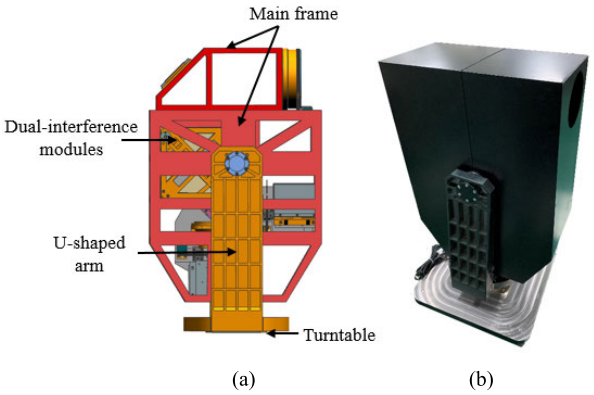

(a) (b)

FIGURE 8. (a) Opto-mechanical model and (b) assembly of imaging spectrometer.

The light emitted by the point source black body entered the imaging spectrometer after beam expansion and collimation, and the narrow-band filter was switched by rotating the filter wheel to obtain the corresponding spectral data. The obtained spectral curve of the broad-band interference channel after calibration is shown in Figure 9(a)–(b). The maximum wavenumber drift occurs at a CWL of 8.688 μm (1151 cm^{-1}). The calibration demonstrates a resulting value of 1147.1 cm^{-1} with a deviation of 0.34%. The obtained spectral curve after calibration of the high-resolution interference channel is shown in Figure 9(c)–(d). The maximum wavenumber drift occurred at a CWL of 4.515 μm (2214.8 cm^{-1}), and the calibration value is 2207.7 cm^{-1} and has a deviation of 0.32%.

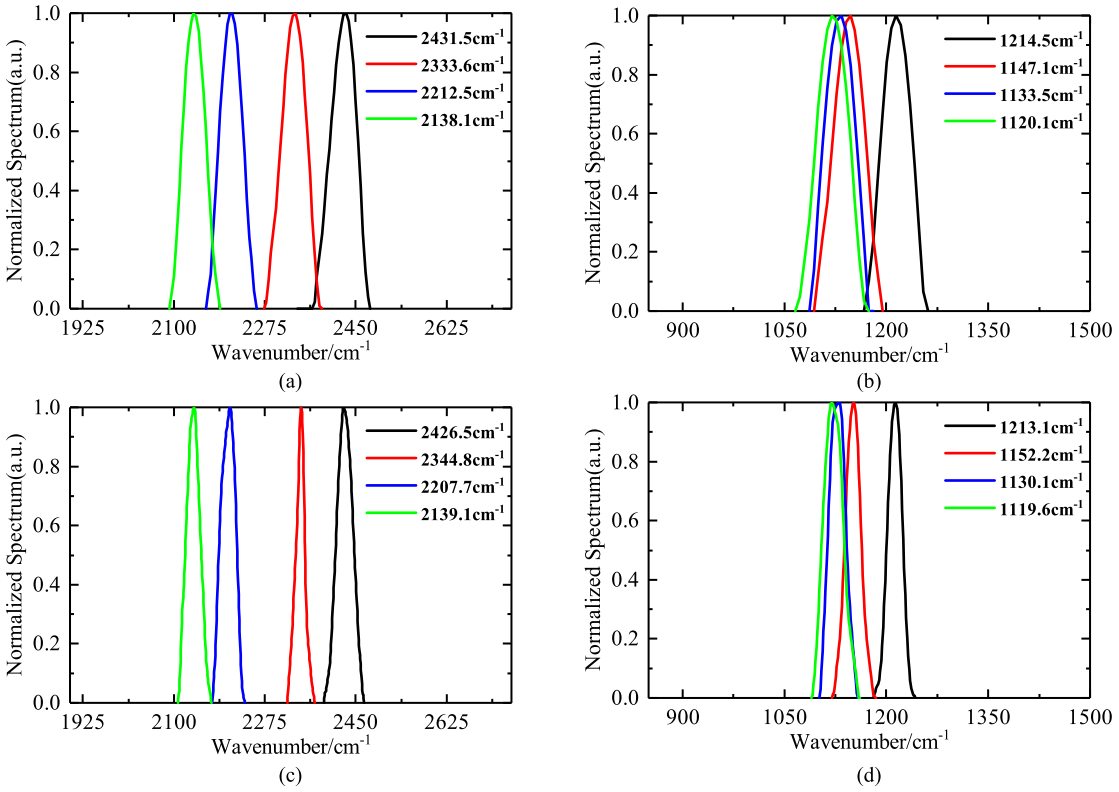

FIGURE 9. Calibration results of the filters (a) MWIR filters in broad-band interference channel, (b) LWIR filters in broad-band interference channel, (c) MWIR filters in high-resolution interference channel, and (d) LWIR filters in high-resolution interference channel.

D. SPECTRAL RESOLUTION

The theoretical value of the spectral resolution is given by Eq. (5), and the actual resolution can be determined by the FWHM of the measured absorption line. The resolution design indexes of the high-resolution interference channel and broad-band interference channel of the imaging spectrometer proposed in this paper are 3.2 cm^{-1} and 50 cm^{-1}, respectively. We placed a liquid cell with a diameter of 1 inch and a length of 3 mm between the point-source black body and the beam expanding collimation system, and then measured the spectrum of acetonitrile in the broad-band interference channel. The measurement results are shown in Figure 10(a). The black line is the standard spectrum, which derives from the chemical database of the Shanghai Institute of Organic Chemistry. The main absorption peak of acetonitrile in the response band is 2246 cm^{-1} and the FWHM is 22 cm^{-1}. The red line is the measured acetonitrile spectrum, the absorption peak is at 2252.4 cm^{-1}, with a wavenumber deviation of 0.27% and a FWHM of 51.5 cm^{-1}. Ammonia was used for testing the high-resolution interference channel. The gas cell had a diameter of 150 mm and a length of 300 mm, and it was placed between the beam expanding collimator system and the optical system. The CWL of the narrowband filter was 8.242 μm and the FWHM was 150 nm. The measurement results are shown in Figure 10(b). The black line is the standard spectrum from the NIST. In the narrow band, the absorption peak of ammonia is at 1215.3 cm^{-1} and the FWHM is 4 cm^{-1}. The red line shows the measured ammonia spectrum, with an absorption peak at 1212.6 cm^{-1}, and its wavenumber deviation is 0.23% and a FWHM of 4.1 cm^{-1}. The above results show that both interference channels have a certain degree of peak position shift and absorption line broadening, which may be caused by factors such as interferogram sampling error and the apodization function.

E. INSTRUMENT SNR

The RMS value of noise on the 100% transmittance line of the air background spectrum in a specific band is calculated, and the reciprocal of the RMS is taken to obtain the SNR of the instrument. We use a point-source black body as a light source, and the SNR calculation is as follows:

$$SNR = \frac{1}{\sqrt{\frac{1}{X}\sum_{i=1}^{X}\left(T_i - \overline{T}\right)^2}} \tag{13}$$

where T is the 100% transmittance line obtained by dividing two background spectra collected under the same conditions in air, $\bar{T}$ is the arithmetic average of the 100% transmittance line, T_i is the value of the i-th channel, and X is the total number of channels. In the spectral response range of this

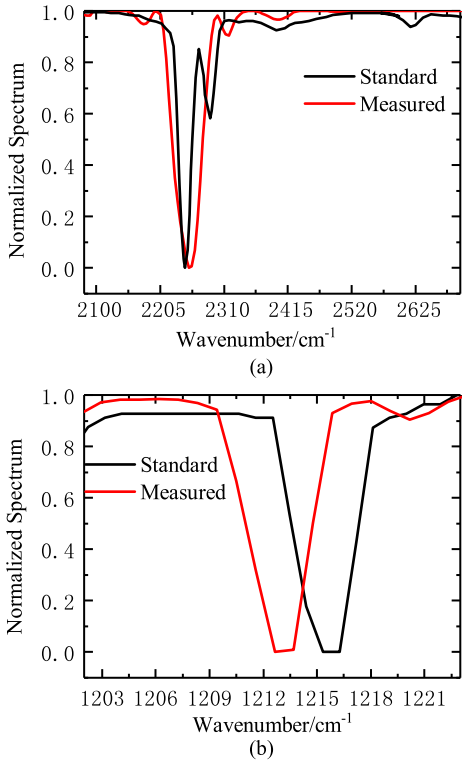

FIGURE 10. Infrared detection experiment with the high-resolution channel and the broad-band channel, (a) normalized transmittance curve of acetonitrile and (b) normalized transmittance curve of ammonia.

TABLE 5. SNR of the instrument.

Interference channel	MWIR	LWIR
Broad band	343	697
High resolution	404	926

instrument, the evaluation band selected for the MWIR was 2100–2200 cm^{-1}, and it was 1075–1250 cm^{-1} for the LWIR. Thirty air background spectra were collected for the two interference channels, and the average 100% transmittance line was taken to avoid random errors caused by a single measurement. In the SNR test of MWIR and LWIR, the temperature of the point source blackbody is set to 375 K and 500 K respectively, the SNR calculation results are shown in Table 5.

F. NOISE EQUIVALENT TEMPERATURE DIFFERENCE

The noise equivalent temperature difference (NETD) is an important indicator to measure the sensitivity of the spectrometer. The theoretical calculation formula of NETD is as follows:

$$NETD = \frac{4F^2\sqrt{\Delta f_n}}{\pi\tau_0\sqrt{Ad}\,\bar{D}^*_\lambda \int_{\lambda_1}^{\lambda_2} \frac{\partial L_\lambda(T_B)}{\partial T_B} d\lambda} \tag{14}$$

where $F = 1.93$ is the working F-number of the optical system, Δf_n is the noise equivalent bandwidth of the detector, τ_0 is the transmittance of the optical system, Ad is the area of a single pixel of the detector, and $\bar{D}^*_\lambda$ is the spectral average detection rate of the detector. $L_\lambda(T_B) = c_1/\left(\lambda^5 \times \left(e^{c_2/\lambda T_B} - 1\right)\right)$ is the spectral radiance of the black body, $c_1 = 3.7415 \times 10^{-16} W \cdot m^2$ is the first radiant constant, $c_2 = 1.4388 \times 10^{-2} m \cdot K$ is the second radiant constant, T_B is the absolute temperature of the black body, λ_1 and λ_2 are the response cut-off wavelengths of the detector. Figure 11 shows that when the absolute temperature of the black body is 300 K, the NETD values of the MWIR and LWIR channels are 0.066 K and 0.129 K, respectively.

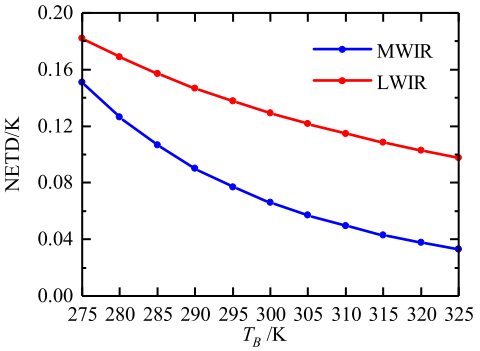

FIGURE 11. NETD of MWIR and LWIR channels.

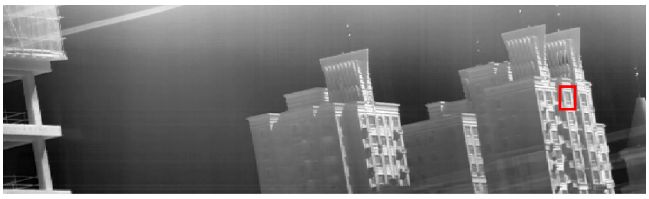

FIGURE 12. MWIR panoramic image based on small-step micro-mirror.

G. IMAGING TEST

The imaging test on the target area was performed at a distance of 800 m. The scanning angle interval ω was determined by the FOV of the instrument and the number of steps N, $\omega = FOV/N = 2.75°/160 = 61.875''$, and 300 frames of interference images were obtained. The feature-based image stitching method was used to cut and stitch the images on the 0-level sub-step in the obtained interference image sequence. The image fusion algorithm eliminates gaps caused by step stitching, and finally leads to a high-resolution panoramic image of the target area, as shown in the Figure 12. The calculation formula for the spatial pixel resolution(SPR) of the optical system is as follows:

$$SPR = \frac{pH}{f'} \tag{15}$$

where $f' = 200$ mm is the focal length of the optical system, $p = 30\ \mu$m is the pixel size, and $H = 800$ m is the detection distance, and $SPR = 0.12$ m. We choose the window as the reference object for the resolution test, as shown in the red rectangular area in Figure 12. The number of pixels that it

occupies in the height direction is 13, and the actual window height is about 1.6 m. It can be calculated that the actual spatial resolution of the instrument is about 0.123 m. The image shows high-throughput and a high-resolution imaging quality, which meet the design index requirements.

V. CONCLUSION

The imaging spectrometer proposed in this paper simultaneously functioned in the MWIR and LWIR. The common-aperture telescope adopted a three-piece lens structure, which minimized broad-band achromatic aberration while maintaining a compact optical system with high throughput. The a thermal design of the instrument in a temperature range of -20 to 60 °C was achieved by the combination of active mechanical and passive optical a thermalization. The standard deviation of the step heights of the designed small-step and large-step micro-mirrors were less than 0.0307 and 0.0413 μm, respectively, which ensured accurate modulation of the OPD. The design of the dual-interference channels module led to a compact system with a stable interference system. The imaging capabilities and spectral capabilities of the instrument were tested and low-distortion, high-throughput, and high-spatial-resolution panoramic images were obtained by stitching the 0-level sub-step images together. The calibrated accuracy of the broad-band and the high-resolution interference channels were better than 0.34% and 0.32%, respectively. The infrared spectra of acetonitrile and ammonia were measured, and accuracy of the measured absorption peak positions were within 0.27% and 0.23% respectively. The measured spectral resolutions of the two interference channels were 51.5 and 4.1 cm^{-1}, respectively. The SNR of the instrument for the two interference channels and two bands were determined, and further evaluation has been planned to be carried out in our future work.

REFERENCES

[1] J. L. Hall, R. H. Boucher, D. J. Gutierrez, S. J. Hansel, B. P. Kasper, E. R. Keim, N. M. Moreno, M. L. Polak, M. G. Sivjee, D. M. Tratt, and D. W. Warren, "First flights of a new airborne thermal infrared imaging spectrometer with high area coverage," *Proc. SPIE*, vol. 8012, May 2011, Art. no. 801203.
[2] P. Z. Mouroulis and R. O. Green, "Review of high fidelity imaging spectrometer design for remote sensing," *Opt. Eng.*, vol. 57, no. 4, 2018, Art. no. 040901.
[3] A. F. H. Goetz, "Three decades of hyperspectral remote sensing of the Earth: A personal view," *Remote Sens. Environ.*, vol. 113, pp. 5–16, Sep. 2009.
[4] P. S. Thenkabail, "Water productivity mapping methods using remote sensing," *J. Appl. Remote Sens.*, vol. 2, no. 1, Nov. 2008, Art. no. 023544.
[5] R. M. Levenson and J. R. Mansfield, "Multispectral imaging in biology and medicine: Slices of life," *Cytometry A*, vol. 69A, no. 8, pp. 748–758, 2006.
[6] F. Sigernes, M. Syrjäsuo, R. Storvold, J. Fortuna, M. E. Grøtte, and T. A. Johansen, "Do it yourself hyperspectral imager for handheld to airborne operations," *Opt. Exp.*, vol. 26, no. 5, pp. 6021–6035, 2018.
[7] D. G. Winters, P. Schlup, and R. A. Bartels, "Highly achromatic Fourier-transform spectrometer," *Opt. Exp.*, vol. 15, no. 3, pp. 1361–1368, 2007.
[8] F. M. Reininger, "The application of large format, broadband quantum well infrared photodetector arrays to spatially modulated prism interferometers," *Infr. Phys. Technol.*, vol. 42, nos. 3–5, pp. 345–362, 2001.
[9] K. Möller, "Wave-front-dividing array interferometers without moving parts for real-time spectroscopy from the IR to the UV," *Appl. Opt.*, vol. 34, no. 9, pp. 1493–1501, 1995.
[10] Y. B. Ji, J. Q. Liang, and Z. Z. Liang, "Optical desgin of infrared bispectrum Fourier transform imaging spectrometer," *Acta Opt. Sin.*, vol. 38, no. 3, 2018, Art. no. 0322001.
[11] S. Wang and B. Xiangli, "Research of spectrum signal-to-noise ratio of large aperture static imaging spectrometer," *Spectrosc. Spect. Anal.*, vol. 34, no. 3, pp. 851–856, 2014.
[12] N. Matallah, H. Sauer, F. Goudail, J. C. Fontanella, Y. Ferrec, J. Taboury, and P. Chavel, "Design and first results of a Fourier transform imaging spectrometer in the 3-5 μm range," *Proc. SPIE*, vol. 8167, Sep. 2011, Art. no. 816715.
[13] Y. Tingyu, Z. Chunmin, Z. Jirui, Q. Naicheng, and T. Cuncun, "High resolution channeled imaging spectropolarimetry based on liquid crystal variable retarder," *Opt. Exp.*, vol. 26, no. 8, pp. 10382–10391, 2018.
[14] C. Zhang, Q. Li, T. Yan, T. Mu, and Y. Wei, "High throughput static channeled interference imaging spectropolarimeter based on a Savart polariscope," *Opt. Exp.*, vol. 24, no. 20, pp. 23314–23332, 2016.
[15] M. H. Köhler, T. T. Nguyen, P. Kienle, X. Dong, M. Schardt, M. Jakobi, and A. W. Koch, "Hyperspectral imager for the mid-infrared spectral range using a single-mirror interferometer and a windowing method," *OSA Continuum*, vol. 2, no. 11, p. 3212, 2019.
[16] M. Schardt, P. J. Murr, M. S. Rauscher, A. J. Tremmel, B. R. Wiesent, and A. W. Koch, "Static Fourier transform infrared spectrometer," *Opt. Exp.*, vol. 24, no. 7, pp. 7767–7776, 2016.
[17] M. Köhler, M. Schardt, M. Rauscher, and A. Koch, "Gas measurement using static Fourier transform infrared spectrometers," *Sensors*, vol. 17, no. 11, p. 2612, Nov. 2017.
[18] M. H. Köhler, S. S. Naßl, P. Kienle, X. Dong, and A. W. Koch, "Broadband static Fourier transform mid-infrared spectrometer," *Appl. Opt.*, vol. 58, no. 13, pp. 3393–3400, 2019.
[19] H. Nyquist, "Certain factors affecting telegraph speed," *Bell System Tech. J.*, vol. 3, no. 2, pp. 324–346, Apr. 1924.
[20] C. E. Shannon, "Communication in the presence of noise," *Proc. IEEE*, vol. 72, no. 9, pp. 1192–1201, Sep. 1984.
[21] D. L. Cohen, "Performance degradation of a Michelson interferometer when its misalignment angle is a rapidly varying, random time series," *Appl. Opt.*, vol. 36, no. 18, pp. 4034–4042, 1997.

JUN REN was born in Nanjing, Jiangsu, China, in 1994. He received the B.S. degree in material physics from the Yancheng Institute of Technology, China, in 2016. He is currently pursuing the Ph.D. degree in optical with the Changchun Institute of Optics, Fine Mechanics and Physics, Chinese Academy of Sciences, Changchun, China. His current research interests include theoretical analysis and optical design of Fourier transform imaging spectrometer.

JINGUANG LÜ received the B.S. degree from the School of Physics, Jilin University, in 2004, and the Ph.D. degree from Changchun Institute of Optics, Fine Mechanics and Physics, Chinese Academy of Sciences, in 2013. He is currently an Associate Professor and a Master Supervisor with the State Key Laboratory of Applied Optics, Changchun Institute of Optics, Fine Mechanics and Physics, Chinese Academy of Sciences. His research interests include micro optical systems, optical information processing, coherent spectral imaging, and other fields.

BAIXUAN ZHAO was born in Changchun, Jilin, China, in 1993. He received the bachelor's degree in physics from Jilin University, in 2016. He is currently pursuing the Ph.D. degree with the Changchun Institute of Optics, Fine Mechanics and Physics. His main research interests include image processing and spectral reconstruction of Fourier imaging spectrometer.

QIANG WANG received the B.S. degree in electronic science and technology and the Ph.D. degree in optical engineering from Shandong University, in 2011 and 2016, respectively. After his graduate study, he worked as a Postdoctoral Fellow with The Chinese University of Hong Kong and the Max Planck Institute of Quantum Optics. He is currently an Associate Professor with the State Key Laboratory of Applied Optics, Changchun Institute of Optics, Fine Mechanics and Physics, Chinese Academy of Sciences. His recent research interests include laser spectroscopy, optical sensing, and engineering application of trace gas analysis in atmosphere, deep sea, and public health.

YUXIN QIN was born in Mudanjiang, Heilongjiang, in 1985. He received the B.S. degree in optical information science and technology and the M.S. degree in optical engineering from Harbin Engineering University, in 2008 and 2011, respectively. Since 2011, he has been working with the State Key Laboratory of Applied Optics, Changchun Institute of Optics, Fine Mechanics and Physics, Chinese Academy of Sciences. His main research interests include experimental research of infrared spectroscopy instrument optical design and assembly adjustment.

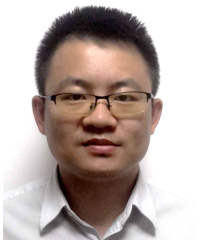

JIN TAO received the B.S. and Ph.D. degrees in measurement technology and instrument from Tianjin University, in 2010 and 2016, respectively. He is currently a Research Associate with the State Key Laboratory of Applied Optics, Changchun Institute of Optics, Fine Mechanics and Physics, Chinese Academy of Sciences. He is also committed to the development and application of micro LED chips and the research of uncooled infrared detection chips based on micro nano resonators.

JINGQIU LIANG received the B.S. degree in professional semiconductor physics and devices from the Department of Electronic Science, Jilin University, in 1984, and the Ph.D. degree from the Changchun Institute of Optics, Fine Mechanics and Physics, Chinese Academy of Sciences, in 2003. She is currently a Professor with the Changchun Institute of Optics, Fine Mechanics and Physics, Chinese Academy of Sciences. Her research interests include micro optical electro mechanical systems (MOEMS) and micro-structure optics, micro Fourier transform spectrometer, Fourier transform imaging spectrometer, micro LED arrays, and devices in visible light communication systems.

WEIBIAO WANG was born in Yangzhou, Jiangsu. He received the Ph.D. degree from the Changchun Institute of Optics, Fine Mechanics and Physics, Chinese Academy of Sciences, in 1999. He is currently a Doctor, a Researcher, and a Doctoral Supervisor. He is also a Researcher with the Changchun Institute of Optics, Fine Mechanics and Physics, Chinese Academy of Sciences. His research interests include photonic crystal and micro-nano photonics, LED array chip integration and application, and field emission materials and electron emission characteristics.